Published in final edited form as:
Int J Radiat Oncol Biol Phys. 2012 November 1; 84(3): e393–e399. doi:10.1016/j.ijrobp.2012.05.005.

^{64}Cu-ATSM pharmacokinetics in FaDu xenograft tumors and correlation with microscopic markers of hypoxia

Keisha C. McCall, PhD[1], **John L. Humm, PhD**[1], **Rachel Bartlett, PhD**[1], **Megan Reese, MS**[2], and **Sean Carlin, PhD**[2]

[1]Department of Medical Physics, Memorial Sloan-Kettering Cancer Center, New York, NY, USA

[2]Department of Radiochemistry & Imaging Sciences Service, Department of Radiology, Memorial Sloan-Kettering Cancer Center, New York, NY, USA

Abstract

Purpose—The behavior of ^{64}Cu-ATSM in hypoxic tumors was examined through a combination of *in vivo* dynamic PET imaging, and *ex vivo* autoradiographic and histological evaluation using a xenograft model of H&N squamous cell carcinoma.

Methods and Materials—^{64}Cu-ATSM was administered during dynamic PET imaging, and temporal changes in ^{64}Cu-ATSM distribution within tumors were evaluated for at least 1 h and up to 18 h. Animals were sacrificed at either 1 h (cohort A) or after 18 h (cohort B) post-injection of radiotracer and autoradiography performed. *Ex vivo* analysis of microenvironment sub-regions was conducted by immunohistochemical staining for markers of hypoxia (Pimonidazole Hydrochloride) and blood flow (Hoechst-33342).

Results—Kinetic analysis revealed rapid uptake of radiotracer by tumors. The net influx (K_i) constant was twelve-fold that of muscle, while the distribution volume (V_d) was five-fold. PET images showed large tumor-to-muscle ratios, which continually increased over the entire 18 h course of imaging. However, no spatial changes in ^{64}Cu-ATSM distribution occurred in PET imaging after 20 minutes post-injection. Microscopic intratumoral distribution of ^{64}Cu-ATSM and Pimonidazole were not correlated at 1 h or after 18 h post-injection, and neither was ^{64}Cu-ATSM and Hoechst-33342.

Conclusions—The oxygen partial pressures at which ^{64}CuATSM and Pimonidazole are reduced and bound in cells are theorized to be distinct and separable. However, this study demonstrated that microscopic distributions of these tracers within tumors are independent. Nonetheless, researchers have shown ^{64}Cu-ATSM uptake to be specific to malignant expression, and this work has also demonstrated clear tumor targeting by the radiotracer.

Keywords

Hypoxia imaging; Cu-ATSM PET; ATSM

Corresponding author: Sean Carlin, PhD., Radiochemistry & Imaging Sciences Service, Department of Radiology, Memorial Sloan-Kettering Cancer Center, 1275 York Avenue, New York, NY, 10065, USA, carlins@mskcc.org.

Conflict of Interest: None

Introduction

As early as 1987, Rasey *et al.* proposed PET imaging to quantify tumor hypoxia using ^{18}F-fluoromisonidazole (^{18}F-FMISO), a member of the 2′-nitroimidazole family of compounds (1). However, ^{18}F-FMISO has inherent limitations for *in vivo* hypoxia imaging due noisy images due to slow uptake and blood clearance (2). Thus for hypoxia specificity, late imaging times post-injection are needed, which result in noisy PET images. The desire for a radiotracer that rapidly produces high signal intensity PET images has motivated investigations of the highly lipophilic bis(thiosemicarbazone) compounds, specifically Copper-diacetyl-bis(N^4-methylthiosemicarbazone) (Cu-ATSM) (3).

The mechanism of uptake of Cu-ASTM in tumors was believed to be hypoxia specific, as partial dependent Cu-ATSM uptake was reported in 9L gliosarcoma preclinical models pressure of oxygen (pO_2) using hydralazine and inhaled oxygen content to manipulate average pO_2 values in tumor tissue (4). Moreover, early clinical trials found SUV of Cu-ASTM to be prognostic for radiotherapy outcome in lung (5), cervical (6), and rectal (7) cancers. However, distinct cell-line dependency in ^{64}Cu-ATSM uptake rates have been shown *in vitro* (8, 9), and tumor model dependencies were also revealed for *in vivo* PET imaging (10). Study of R3327-AT prostate tumor models showed reverse PET distribution of ^{64}Cu-ATSM versus ^{18}F-FMSIO at early times post-injection, but showed improved agreement between the radiotracers in late images acquired 18 h post-injection of ^{64}Cu-ATSM. Other studies suggest that ^{64}Cu-ATSM may not be hypoxia specific in prostate cancer models in general (9). However, a FaDu H&N tumor model showed close visual agreement between ^{18}F-FMISO and ^{64}Cu-ATSM PET images at both the early and late time-points (10). The apparent agreement between ^{18}F-FMISO and ^{64}Cu-ATSM PET images with little evolution in the macroscopic ^{64}Cu-ATSM distribution led to the interpretation of rapid hypoxia-specific localization of ^{64}Cu-ATSM within these types of cancers (10).

Interpretation of nuclear images of tumor hypoxia may be complicated by difficulties in determining to what extent radiotracer distribution is determined by “supply” (*i.e.* perfusion, vascularity) or “demand” (*i.e.* pO_2 level). Yet, the rapid cellular uptake of Cu-ATSM, as observed in preclinical and clinical studies, has led to clinical PET protocols adopting early imaging times of between 20 min to 50 min post-injection. However, it remains to be determined whether early Cu-ATSM PET imaging is significantly affected by non-specific radiotracer delivery, and whether delaying acquisition to late time-points, when vascular clearance has completed, would provide a hypoxia specific image. In the FaDu tumor model, the assumption of rapid and hypoxia specific ^{64}Cu-ATSM accumulation had not been validated. The association of Cu-ATSM PET signals with hypoxia specific accumulation or with vascular delivery and perfusion cannot be determined without studying the pharmacokinetics of the radiotracer. Also, the limited spatial resolution of PET did not provide sufficient information about hypoxia specific *vs.* non-specific accumulation of Cu-ATSM within the tumor microenvironment. To answer these questions, we performed kinetic PET imaging of FaDu tumor models followed by digital autoradiography and immunohistochemical analysis in animals sacrificed at early (1 h) and late (after 18 h) time-points post-injection of ^{64}Cu-ATSM.

Methods and Materials

Tumor models

Subcutaneous xenografts of FaDu human H&N tumors were grown in nude rats in accordance with an Institutional Animal Care Committee (IACUC) protocol. 1×10^6 tumors cells were implanted in the right hind limb of each animal, and tumors allowed to grow for 2

to 3 weeks until their longest diameters reached 20 mm ± 4 mm standard deviation, with an average tumor volume of approximately 3 cm^3. Animals were then divided into equally sized ($n = 4$) cohorts A and B; each cohort differing only in the duration of PET imaging protocols and time of sacrifice (*i.e.* early or late times post-injection).

Radiotracer and histochemical marker administration

During *in vivo* PET imaging, radiolabeled Cu(II)-diacetyl-bis(N(4)-methylthiosemicarbazone) (^{64}Cu-ATSM) was administered, as an intravenous bolus of 43.3 MBq ± 8.4 MBq standard deviation. The injected volume of the radiotracer bolus was approximately 350 μL, and injections were followed by a 500 μL saline flush. The ^{64}Cu-ATSM radiotracer had been synthesized at the Cyclotron-Radiochemistry core facility of the institution with radiochemical purity of 99% as assessed by instant thin layer chromatography. High specific activity ^{64}Cu radioisotope was obtained from Washington University School of Medicine, and ligand synthesis and labeling was done using published methods (3). The longer radiological half-life of ^{64}Cu ($\tau = 12.6$ h) allowed negligible difference in noise between early and late emission images. For subsequent *ex vivo* immunohistochemical analysis, both cohorts were intravenously administered 80 mg/kg of Pimonidazole Hydrochloride (Pimonidazole) at 3 hours prior to sacrifice, and 15 mg/kg Hoechst-33342 at 5 minutes prior to sacrifice.

PET imaging

All PET imaging was performed on the Focus 120™ (Siemens Medical Systems, USA) preclinical microPET® system and animals were anesthetized by isoflurane inhalation. Cohort A were scanned in a 90-minute dynamic (list mode) PET sequence, and then re-scanned for 10-minute PET acquisitions at 6 h and 18 h after the injection of ^{64}Cu-ATSM. Cohort B underwent a 50-minute dynamic PET sequence only. Cohort A required additional immobilization via a molded foam bed and skin tattooing for consistency in positioning of the tumor between the early and late imaging sessions. PET acquisitions were initiated ~10 s prior to administering the bolus to ensure adequate sampling of the initial venous passage of the radiotracer. The list-mode data then were binned into time-frames designed to finely sample the early phases of the pharmacokinetics. Ordered Subset Expectation Maximization (OSEM) with calculated attenuation-correction was used for image reconstruction.

Pharmacokinetic analysis

Regions of interest (ROI) within the tumor and normal tissue were delineated using PET images acquired at 40 min post-injection. Necrotic tumor tissue was excluded from pharmacokinetic analysis by delineating only voxels ≥ 30% of the maximum tumor signal. The muscle ROI was identified within the left hind leg. The venous ROI was a lateral vein at the base of the tail and delineated in PET images acquired within the first 10 s post-injection. Time activity curves (TAC) were derived from the mean activity concentration within each ROI at each time-frame of the dynamic PET sequence. Tissue activity concentration functions (C_t), the TAC of tumor or muscle ROI, were then compared to venous input functions (C_p), which was estimated as the TAC for whole blood in the venous ROI. Influx-constants or steady-state trapping rates (K_i) were calculated by linear regression analysis of Patlak (11) plots of C_t/C_p ratios versus normalized time integrals of C_p. The distribution volume (V_d) were also calculated by Logan plots (12) of time integrals of C_t and C_p.

Ex vivo autoradiography, histology, and immunohistochemistry

Immediately after sacrifice, a 30 gauge angiocatheter was placed in a central tumor location perpendicular to the PET imaging plane, as a fiducial marker for *ex vivo* image registration.

The tumors were removed with the angiocatheter *in situ*, embedded in specimen mounting medium, frozen, and sliced into 10-μm-thick tissue sections. Two tissue sections per animal were used for microscopic imaging, which correspond to PET image locations with the anterior and posterior or the superior and inferior halves of the tumor.

Digital autoradiographs of ^{64}Cu-ATSM microdistributions were obtained by exposing tissue sections to a phosphor imaging screen for 12 h at −20°C. Immunofluorescence staining of Pimonidazole and Hoechst-33342 was carried out, and the tissue sections imaged by fluorescence microscopy. General histology was also assessed by hematoxylin and eosin (H&E) staining. Autoradiographic and microscopic images were co-registered using image processing software by aligning the fiducial marks and tissue boundaries. Image registrations were evaluated to maximize the normalized mutual information criterion between the microscopic images. Co-registered microscopic images were then resampled down to the 50-μm pixel-size of autoradiographs, using a box filter to retain contrast and relative pixels intensities.

Spatial analysis

None of the extrinsic markers was observed to pool in necrotic regions, and co-distributions within muscle were not relevant to this study. Therefore, analysis of spatial correlation was selectively restricted to viable tumor as identified by H&E histology, excluding necrosis, muscle and other non-tumor tissue. The relationships between microdistributions of ^{64}Cu-ATSM, Pimonidazole, and Hoechst-33342 within viable tumor regions were quantified by Spearman rank correlation coefficients (Spearman's ρ). To facilitate visualization of scattergrams and to evaluate statistical trends, the several thousand pixel-values of each microdistribution image were binned into deciles (13).

Results

PET images indicated significantly higher accumulation of ^{64}Cu-ATSM in tumors than in muscle tissue ($p < 0.01$). Figure 1 shows a sequence of PET images of a typical tumor, and spans the time-frame from 20 min to 18 h post-injection. At 20 min, tumors exhibited four-fold higher ^{64}Cu-ATSM uptake than muscle, and tumor-to-muscle ratios continued to increase over time, reaching twelve-fold at 18 h. Due to hepatobiliary clearance of ^{64}Cu-ASTM metabolites, gut uptake became apparent in later PET images and peaked at 6 h post-injection in figure 1.

Digital autoradiography confirmed higher accumulation of radiotracer within tumor cells as compared to muscle. In figure 2, autoradiographs were compared to histology, and show an example of microdistributions of ^{64}Cu-ATSM within a tissue section. Qualitatively, ^{64}Cu-ASTM concentrations in viable (non-necrotic) tumor tissue were visibly higher than the surrounding muscle. Additionally, microdistributions of radiotracer were heterogeneous within the viable tumor region.

The mean activity within PET voxels, PET_{mean}, of tumor and muscle regions was used to quantify net ^{64}Cu-ATSM retention in the tissues. TACs in figure 3(a) was generated by plotting the PET_{mean} values of dynamic PET images after correcting for radiological decay between the imaging time-points. PET_{mean} values within muscle remained statistically constant ($p > 0.01$) after 20 min post-injection. In contrast, PET_{mean} in tumors rapidly increased within the first minute, reaching a pseudo-plateau then continued to increase at a much slower rate, indicating that net ^{64}Cu-ATSM retention within tumors did not reach an absolute steady state even at many hours post-injection. Despite continual increase in PET_{mean}, macroscopic distributions of radiotracer within the PET images remained stable, with high spatial correlation (Pearson's $r > 0.6$) between PET images of the tumors acquired

at 18 h and at 20 min post-injection. The stable macroscopic distributions were also apparent in figure 1.

Pharmacokinetic analysis

Patlak and Logan plots were generated for each rat, and linear regression analysis was used to fit data points that corresponded to a time interval spanning 3 min through 50 min post-injection. The time interval for regression analysis was selected because the sharply rising initial segment of Patlak plots flattened after 3 min and dynamic data for cohorts B only extended to 50 min post-injection. Examples of Patlak and Logan plots and linear regression fits are shown in figure 3(b, c), while table 1 detailed tumor-to-muscle ratios of the pharmacokinetic parameters.

Regression analysis of the Patlak plots often showed marginal to poor fits to a linear line. This can be observed as divergent data points in figure 3(b) and was indicated by low r^2 regression values, especially for muscle ROIs. This indicates that steady state was not reached at 50 min post-injection and that trapping was not irreversible. As a consequence of the poor Patlak fits, the estimate of influx rate, K_i, had wide 95% confidence intervals. For tumors, the 95% confidence intervals about the mean K_i was [2.8×10^{-2} min^{-1} to 3.5×10^{-2} min^{-1}]. For muscle the Patlak fits were slightly worse with a wider 95% confidence interval of [3.0×10^{-3} min^{-1} to 5.0×10^{-3} min^{-1}] about the mean K_i value. In contrast, Logan plots showed distinct linear trends, with r^2 regression values well above 0.9 for both tumor and muscle ROIs; see figure 3(c). Likewise, the pharmacokinetic parameters were better estimated from these plots. The 95% confidence intervals about the mean volume of distribution, V_d, was [1.9 $ml{\cdot}cm^{-3}$ to 2.1 $ml{\cdot}cm^{-3}$] for tumors, and were [0.42 $ml{\cdot}cm^{-3}$ to 0.44 $ml{\cdot}cm^{-3}$] for muscle.

As shown in table 1, all PET values and most pharmacokinetic parameters were significantly greater within tumor than in muscle ($p < 0.01$). At the 95% confidence interval, the K_i values for tumors of ^{64}Cu-ATSM was five-were estimated to be between seven-fold to eleven-fold that of muscle, while V_d fold greater for tumors than muscle tissue. Within the 50 min post-injection interval, PET_{mean} within tumors were also five-fold greater. However, the effective washout rate of ^{64}Cu-ATSM, χ_2, was indistinguishable ($p = 0.02$) between tumor and muscle. Even though effective washout rates were similar, ^{64}Cu-ATSM concentration within tumors were observed to increase steadily over time. This was indicated by the slope of TACs in figure 3(a), and in table 1, ratios of PET_{mean} within tumors versus muscle continually increased reaching twelve-fold at 18 h.

Spatial analysis

Scattergram analysis of autoradiographs and immunohistochemical slides showed a random relationship between microdistribution of ^{64}Cu-ATSM and accumulation of Pimonidazole, within tumors. Macroscopic PET images in figure 1 were similar over time; nonetheless, figure 4 and figure 5 illustrate that changes did occur in ^{64}Cu-ATSM microdistributions between early and late time-points.

In figure 4, no significant trend was found between ^{64}Cu-ATSM and Pimonidazole at either time-point. Across both cohorts, Spearman's ρ values were not significantly greater than zero ($p > 0.05$) for seven of the sixteen tumor sections analyzed. Of the nine data sets that showed significant Spearman's ρ values ($p \leq 0.05$), six showed negative correlation while the other three showed positive correlation. Figures 4(c), 4(d) show examples of bimodal behavior observed between Pimonidazole and ^{64}Cu-ATSM microdistributions at early time-points, with a positive slope at very low ^{64}Cu-ATSM values followed by a negative slope. Figures 4(a) and 4(b) are examples of the monotonic trends at late time-points, but note that

both positive and negative correlations were observed. Inconsistent spatial relationships between late ^{64}Cu-ATSM and Pimonidazole were even evident among different tissue sections of the same tumor. Likewise, no visual pattern can be observed between Pimonidazole fluorescence images and ^{64}Cu-ATSM autoradiographs at the early time-points of figure 5(c), or the late time-points of figure 5(g). Strong anti-correlation was found between Pimonidazole and Hoechst-33342 microdistributions (Spearman's $\rho > -0.9$, $p \ll 0.05$), and this can also be observed in figures 5(d) and 5(h). A significant positive relationship was found between early ^{64}Cu-ATSM and Hoechst-33342 (Spearman's $\rho > 0.9$, $p \ll 0.05$); however, no correlation was found after 18 h post-injection. In figure 5, early ^{64}Cu-ATSM appears co-distributed with the blood flow marker.

No relationship was found between elevated ^{64}Cu-ATSM signal within the tumor and the hypoxic fraction measured by Pimonidazole positive staining. Corrected for necrosis, the hypoxic fraction within the tumor sections was calculated as the fraction of the viable tumor that was Pimonidazole positive. Positive staining was determined by visual inspection, and corresponded to a color threshold of 1/3 of the 8-bit pixel maximum. Likewise, elevated ^{64}Cu-ATSM signal was defined as autoradiography signals greater than 1/3 of pixel saturation level. The hypoxic fraction of the sixteen tumor samples was 28% and ranged from 16% to 51%. At 1 h, the average ^{64}Cu-ATSM signal in the tumor sections was 55%, and at 18 h, average ^{64}Cu-ATSM signal was 79%. There was no correlation to hypoxic fractions at the 1 h (Spearman's $\rho = 0.33$, $p = 0.4$), or 18 h (Spearman's $\rho = -0.24$, $p = 0.6$) time-points.

Discussion

Using a xenograft model of H&N squamous cell carcinoma, we observed rapid tumor uptake and retention of radiotracer. Tumor-to-muscle ratios were 4:1 within 20 min post-injection and were still increasing at 18 hr post injection. Yet, this H&N tumor model did not exhibit an evolution of the macroscopic radiotracer distributions in PET imaging, which had been observed in other tumors (10). Comparative autoradiography and immunohistochemical analysis revealed that sub-tumoral distribution of ^{64}Cu-ATSM was not easily interpreted. ^{64}Cu-ATSM and nitroimidazole-based hypoxia tracers (exemplified here by Pimonidazole) have quite different uptake dependencies. At 1 h post injection, the early ^{64}Cu-ATSM showed no correlation to Pimonidazole, but strong positive correlations with Hoechst-33342, indicative of highly perfused regions. Correlation to Hoechst-33342 was not observed with the late ^{64}Cu-ATSM after 18 h; however, there was still no clear correlation to the Pimonidazole hypoxia tracer.

Because of the electrochemical properties of Cu-ATSM (3, 14), quantification of Cu-ATSM PET signals is assumed to provide direct indication of pO_2 levels and hypoxia in tumors. However, the precise mechanism of in Cu-ATSM accumulation remains largely unknown, as Cu-ATSM accumulation occurs under normoxic conditions (8, 15) and is strongly influenced by genetic characteristics that are independent of pO_2 status (8, 9, 16). As such, there is a need to further investigate the pathways of Cu-ATSM transport, to determine if active influx and efflux of Cu-ATSM and its metabolites (*e.g.* protein bound ^{64}Cu) are likely to out-compete pO_2 dependent retention mechanisms. Strong evidence of active influx and efflux of Cu-ATSM by cell membrane proteins has been found in human cancer cells (17), and the expressions of proteins involved in Cu-ATSM transport pathways are likely specific to the cell type. *In vivo* copper homeostasis results in the active transport of protein bound Cu from plasma into tissue within 30 min or less (18), so during a typical PET scan Cu-ATSM metabolites may enter the copper regulation cycle and be actively transported into and out of tumor cells.

Nonetheless, Cu-ATSM PET may provide clinical benefits for tumor demarcation due to large tumor-to-muscle ratios at early times post-injection. Autoradiographs confirmed higher Cu-ATSM levels in viable tumor cells versus stromal and muscle tissue. Cu-ATSM PET has also shown prognostic strengths (5–7), which may be powered by a number of hypoxia-independent factors. Copper homeostasis in malignant cells is often altered to maintain significantly higher copper levels (19), which is linked to cancer progression (20). The potential utility of Cu-ATSM as a tumor imaging agent may lie with its relationship to these characteristics.

Acknowledgments

Grant support: NIH R01 CA84596, R24 CA83084, P01 CA115675 and P50 CA86438; Geoffrey Beene Cancer Research Foundation

Nicholas Ramos of the Lewis Research Laboratory, and the Cyclotron-Radiochemistry Core Facility, Pat Zanzonico, PhD and Valerie Longo of the Animal Imaging Core Facility, Memorial Sloan-Kettering Cancer Center

References

1. Rasey JS, Grunbaum Z, Magee S, et al. Characterization of Radiolabeled Fluoromisonidazole as a Probe for Hypoxic Cells. Radiation Research. 1987; 111:292–304. [PubMed: 3628717]
2. Grunbaum Z, Freauff SJ, Krohn KA, et al. Synthesis and Characterization of Congeners of Misonidazole for Imaging Hypoxia. Journal of Nuclear Medicine. 1987; 28:68–75. [PubMed: 3794812]
3. Fujibayashi Y, Taniuchi H, Yonekura Y, et al. Copper-62-ATSM: A New Hypoxia Imaging Agent with High Membrane Permeability and Low Redox Potential. Journal of Nuclear Medicine. 1997; 38:1155–1160. [PubMed: 9225812]
4. Lewis JS, Sharp TL, Laforest R, et al. Tumor uptake of copper-diacetyl-bis(N(4)-methylthiosemicarbazone): effect of changes in tissue oxygenation. Journal of Nuclear Medicine. 2001; 42:655–661. [PubMed: 11337556]
5. Dehdashti F, Mintun MA, Lewis JS, et al. In vivo assessment of tumor hypoxia in lung cancer with 60Cu-ATSM. European Journal of Nuclear Medicine and Molecular Imaging. 2003; 30:844–850. [PubMed: 12692685]
6. Dehdashti F, Grigsby PW, Mintun MA, et al. Assessing tumor hypoxia in cervical cancer by positron emission tomography with 60Cu-ATSM: Relationship to therapeutic response—a preliminary report. International Journal of Radiation Oncology, Biology, Physics. 2003; 55:1233–1238.
7. Dietz D, Dehdashti F, Grigsby P, et al. Tumor Hypoxia Detected by Positron Emission Tomography with 60Cu-ATSM as a Predictor of Response and Survival in Patients Undergoing Neoadjuvant Chemoradiotherapy for Rectal Carcinoma: A Pilot Study. Diseases of the Colon & Rectum. 2008; 51:1641–1648. [PubMed: 18682881]
8. Burgman P, O'Donoghue JA, Lewis JS, et al. Cell line-dependent differences in uptake and retention of the hypoxia-selective nuclear imaging agent Cu-ATSM. Nuclear Medicine and Biology. 2005; 32:623–630. [PubMed: 16026709]
9. V3vere AL, Lewis JS. Examining the relationship between Cu-ATSM hypoxia selectivity and fatty acid synthase expression in human prostate cancer cell lines. Nuclear Medicine and Biology. 2008; 35:273–279. [PubMed: 18355682]
10. O'Donoghue JA, Zanzonico P, Pugachev A, et al. Assessment of regional tumor hypoxia using 18F-fluoromisonidazole and 64Cu(II)-diacetyl-bis(N4-methylthiosemicarbazone) positron emission tomography: Comparative study featuring microPET imaging, Po2 probe measurement, autoradiography, and fluorescent microscopy in the R3327-AT and FaDu rat tumor models. International Journal of Radiation Oncology*Biology*Physics. 2005; 61:1493–1502.
11. Patlak CS, Blasberg RG, Fenstermacher JD. Graphical Evaluation of Blood-to-Brain Transfer Constants from Multiple-Time Uptake Data. Journal of Cerebral Blood Flow and Metabolism. 1983; 3:1–7. [PubMed: 6822610]

12. Logan J. Graphical analysis of PET data applied to reversible and irreversible tracers. Nuclear Medicine and Biology. 2000; 27:661–670. [PubMed: 11091109]
13. Carlin S, Pugachev A, Sun X, et al. In vivo characterization of a reporter gene system for imaging hypoxia-induced gene expression. Nuclear Medicine and Biology. 2009; 36:821–831. [PubMed: 19720294]
14. Obata A, Yoshimi E, Waki A, et al. Retention mechanism of hypoxia selective nuclear imaging/radiotherapeutic agent Cu-diacetyl-bis-methylthiosemicarbazone) (Cu-ATSM) in tumor cells. Annals of Nuclear Medicine. 2001; 15:499–504. [PubMed: 11831397]
15. Yuan H, Schroeder T, Bowsher JE, et al. Intertumoral differences in hypoxia selectivity of the PET imaging agent 64Cu(II)-diacetyl-bis(N4-methylthiosemicarbazone). Journal of Nuclear Medicine. 2006; 47:989–998. [PubMed: 16741309]
16. Liu J, Hajibeigi A, Ren G, et al. Retention of the Radiotracers 64Cu-ATSM and 64Cu-PTSM in Human and Murine Tumors Is Influenced by MDR1 Protein Expression. Journal of Nuclear Medicine. 2009; 50:1332–1339. [PubMed: 19617332]
17. Price KA, Crouch PJ, Volitakis I, et al. Mechanisms Controlling the Cellular Accumulation of Copper Bis(thiosemicarbazonato) Complexes. Inorganic Chemistry. 2011; 50:9594–9605. [PubMed: 21882803]
18. Turnlund J. Human whole-body copper metabolism. The American Journal of Clinical Nutrition. 1998; 67:960S–964S. [PubMed: 9587136]
19. Margalioth EJ, Schenker JG, Chevion M. Copper and Zinc levels in normal and malignant tissues. Cancer. 1983; 52:868–872. [PubMed: 6871828]
20. Turski ML, Thiele DJ. New Roles for Copper Metabolism in Cell Proliferation, Signaling, and Disease. Journal of Biological Chemistry. 2009; 284:717–721. [PubMed: 18757361]

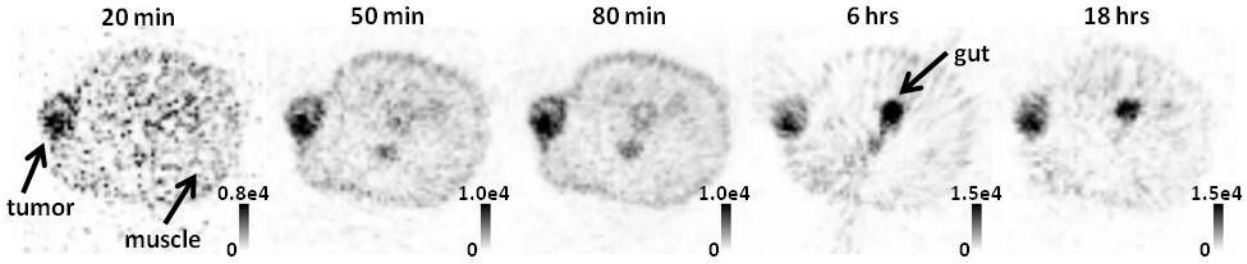

Figure 1.

Dynamic PET image sequence showing an axial slice though a subcutaneous FaDu tumor. Tumor-to-muscle ratio of ^{64}Cu-ATSM accumulation continually increased over the 90-minute imaging sequence; but spatial distribution within the tumor was unchanged. At 6 h and 18 h, hepatobiliary excretion of ^{64}Cu-ATSM metabolites can be noted within the liver (not shown) and gut.

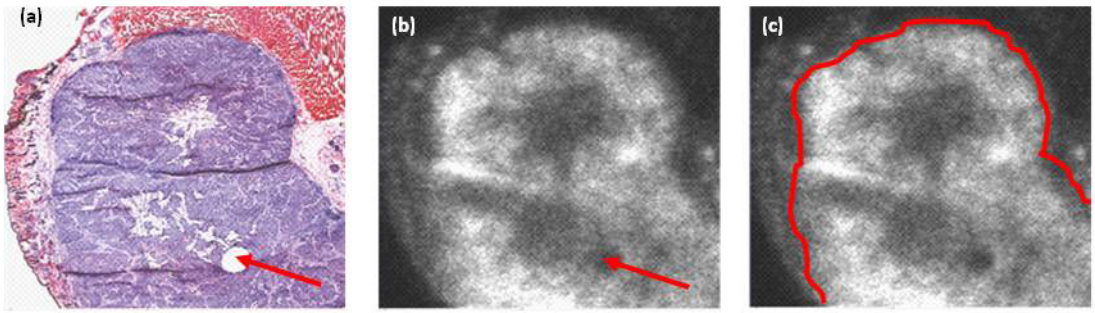

Figure 2.
Histology of FaDu tumor and microdistribution of ^{64}Cu-ATSM. Figures show H&E stained tissue section (a), and autoradiograph of the same section (b), with the tumor delineated (c). Arrows indicate a fiducial mark used for image registration.

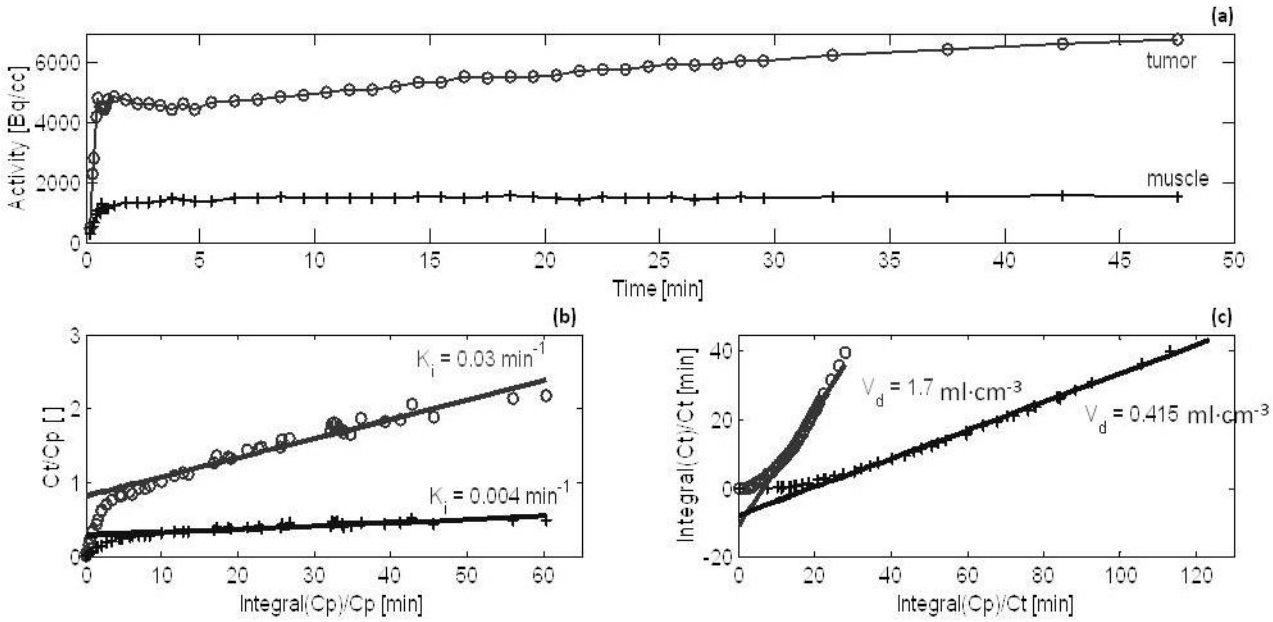

Figure 3.

Graphical pharmacokinetic analysis of the behavior of ^{64}Cu-ATSM within tumors (o), and normal muscle tissues (+) over time. Figures show time activity curves (a), Patlak plots (b), and Logan plots (c) from the analysis of one representative animal.

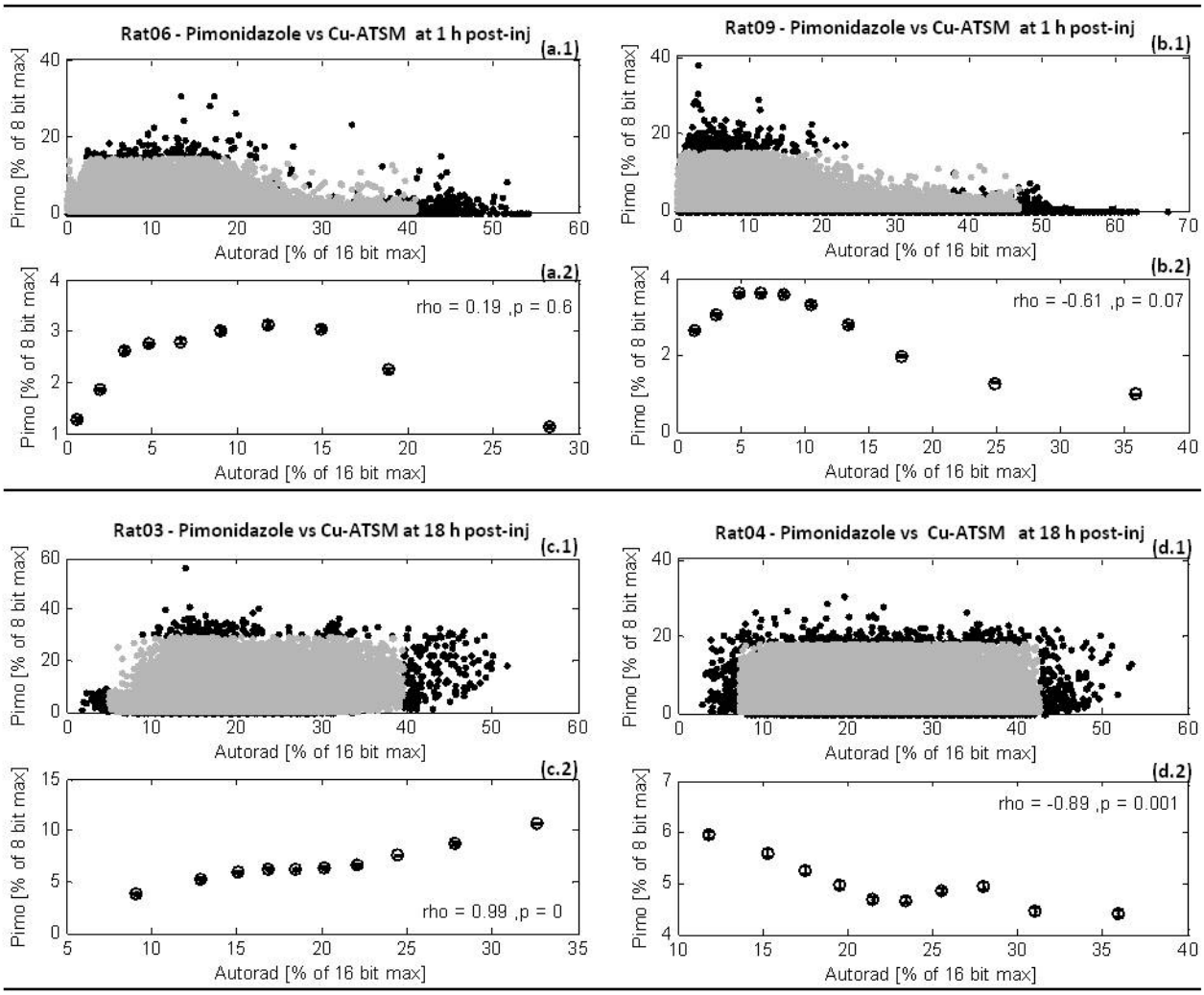

Figure 4.

Scattergrams and correlation analysis of Pimonidazole microscopy, Pimo, *vs.* ^{64}Cu-ATSM autoradiography, Autorad, in four representative tumors. Figures (a) and (b) show Pimo *vs.* early Autorad at 1 h post-injection of ^{64}Cu-ATSM. Figures (c) and (d) show Pimo *vs.* late Autorad at 18 h. The central 99% of pixel values from scattergrams (a.1), (b.1), (c.1), and (d. 1) were binned into deciles for analysis of spatial correlation between the Pimo *vs.* Autorad microdistributions. This correlation analysis is shown in the plots correspondingly labeled (a.2), (b.2), (c.2), and (d.2).

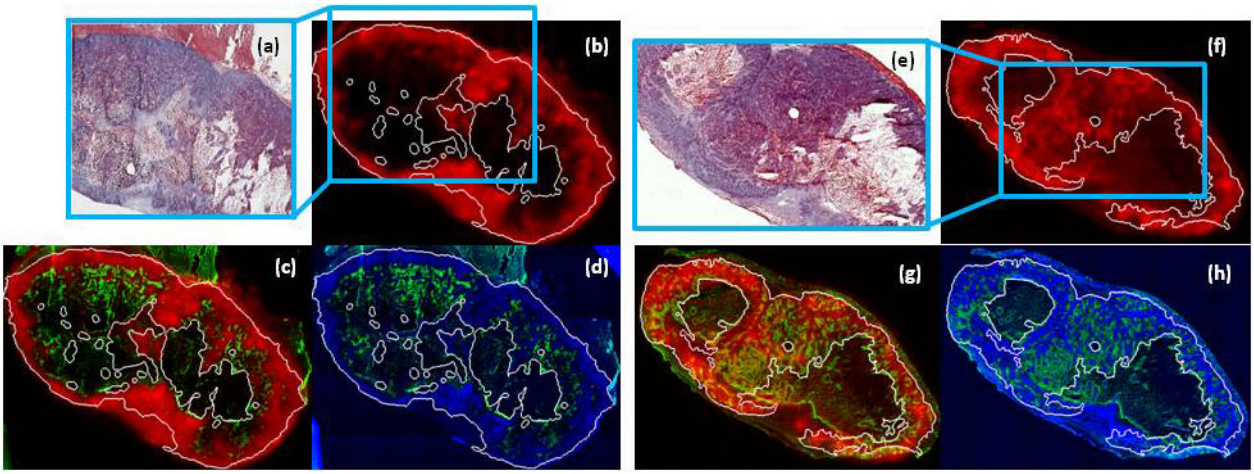

Figure 5.

Microenvironmental features at early and late time-points post injection of ^{64}Cu-ATSM. Figures (a) and (e) are H&E stained tumor histology tissue sections of two FaDu tumors. The viable tumor regions were contoured on H&E histology and are indicated by white lines in the corresponding immunohistochemical and autoradiographic images. Early and late ^{64}Cu-ATSM autoradiographs, at 1 h and after 18 h post-injection, are shown in (b) and (f). Spatial microdistribution of Pimonidazole [green] with the early ^{64}Cu-ATSM [red] is shown in figure (c) and with the late ^{64}Cu-ATSM in figure (g). Figures (d) and (h) show Pimonidazole [green] and Hoechst-33342 [blue] microdistributions.

Table 1

Tumor-to-muscle ratios of ^{64}Cu-ATSM pharmacokinetic parameters and mean PET values.

		Tumor-to-muscle ratio							
		V_d	**χ_2**	**K_i**	**PET_{mean} (20min)**	**PET_{mean} (30min)**	**PET_{mean} (40min)**	**PET_{mean} (80min)**	**PET_{mean} (18h)**
cohort A	**Rat01**	4.16	0.70	6.12	3.72	4.08	4.16	4.92	17.07
	Rat02	6.70	1.01	7.40	6.47	6.58	6.86	7.49	11.41
	Rat03	4.18	0.88	4.79	NA†		4.18	4.35	10.70
	Rat04	3.48	0.82	4.29	3.37	3.41	3.58	3.98	9.50
cohort B	**Rat06**	4.22	0.44	14.54	4.28	4.64	4.94	NA‡	
	Rat07	7.00	0.63	12.77	6.86	7.58	7.84		
	Rat08	4.45	0.42	9.60	4.15	4.30	4.64		
	Rat09	4.07	0.61	7.60	3.92	4.35	4.48		
sample statistics	**mean**	***4.78***	***0.69***	***8.39***	***4.68***	***4.99***	***5.09***	***5.18***	***12.17***
	± std error	*± 0.46*	*± 0.07*	*± 1.30*	*± 0.53*	*± 0.57*	*± 0.52*	*± 0.79*	*± 1.68*
	p value	**2.E-04**	**2.E-02** *	**2.E-04**	**8.E-06**	**5.E-06**	**7.E-07**	**5.E-04**	**4.E-03**

NA† indicates missing data where the dynamic scan of Rat03 was briefly interrupted by a software failure.

NA‡ indicates unavailable data at the late time-points for cohort B (sacrificed at 1 h).

* indicates a lack of statistical significance.